SPACE ROBOTS

A robotic device using gecko-inspired adhesives can grasp and manipulate large objects in microgravity

Hao Jiang,[1]* Elliot. W. Hawkes,[1] Christine Fuller,[2] Matthew A. Estrada,[1] Srinivasan A. Suresh,[1] Neil Abcouwer,[2] Amy K. Han,[1] Shiquan Wang,[1] Christopher J. Ploch,[1] Aaron Parness,[2] Mark R. Cutkosky[1]

Grasping and manipulating uncooperative objects in space is an emerging challenge for robotic systems. Many traditional robotic grasping techniques used on Earth are infeasible in space. Vacuum grippers require an atmosphere, sticky attachments fail in the harsh environment of space, and handlike opposed grippers are not suited for large, smooth space debris. We present a robotic gripper that can gently grasp, manipulate, and release both flat and curved uncooperative objects as large as a meter in diameter while in microgravity. This is enabled by (i) space-qualified gecko-inspired dry adhesives that are selectively turned on and off by the application of shear forces, (ii) a load-sharing system that scales small patches of these adhesives to large areas, and (iii) a nonlinear passive wrist that is stiff during manipulation yet compliant when overloaded. We also introduce and experimentally verify a model for determining the force and moment limits of such an adhesive system. Tests in microgravity show that robotic grippers based on dry adhesion are a viable option for eliminating space debris in low Earth orbit and for enhancing missions in space.

INTRODUCTION

Space presents new challenges for grasping and manipulation. One urgent application is to capture debris in orbit. The amount of space debris has been growing rapidly, with more than 20,000 objects larger than 10 cm in diameter orbiting Earth at speeds of up to 28,000 km/hour (*1*). The status of debris is closely monitored and reported in (*2*). Collisions between in-service satellites and debris can cause millions of dollars of losses. Further, collisions can trigger a chain reaction that creates even more debris. Capturing and recycling debris can keep satellites safe and potentially reduce costs (*3*). Unlike nets, harpoons, and other systems proposed for capturing objects in space (*4*, *5*), a robot with a gripper can apply controlled forces and motions (*6*). This capability allows robots to perform inspection and repair tasks, thereby protecting humans from dangerous extravehicular exposure (*7*). A climbing robot can reach more locations and is potentially more versatile than a robotic arm and camera (*8*, *9*). The robot needs to grip structures firmly and manipulate its body to perform desired tasks, some of which may require exerting substantial forces on the structure.

The current approach to grasping objects in space is to use a gripper or grappling tool that docks to designed features on cooperative targets (*10*, *11*). However, many retired satellites, solar panels, fuel tanks, and rocket bodies are not cooperative and do not have features for docking; rather, they have flat or curved exterior surfaces. Even for active satellites and space stations, graspable features are sparse. Traditional grasping methods usually require either (i) opposed fingers or arms that compress two faces on the object to generate adequate friction forces or (ii) an appendage that wraps around an object or handle to hold it (*12*). Thus, for either a debris grappling mission with multiple uncooperative targets or an inspection task on the surface of a large spacecraft, a gripper may become complex and bulky if one attempts to grasp by traditional means (*13*). Most of the current noncooperative satellite servicing and grappling missions are still in proposal stages (*14*–*16*).

[1]Department of Mechanical Engineering, Stanford University, Stanford, CA 94305, USA. [2]NASA Jet Propulsion Laboratory, Pasadena, CA 91011, USA.
*Corresponding author. Email: jianghao@stanford.edu

An alternative approach is to grasp surfaces directly. The traditional surface-grasping technologies of suction and chemical adhesion cannot be used in space owing to vacuum, radiation, and temperature constraints. Magnetism is ineffective on nonferrous surfaces such as glass or aluminum. However, two other surface-grasping technologies—passive dry adhesion based on van der Waals forces and active electrostatic adhesion—are space-compatible and relatively insensitive to surface materials (*8*, *17*–*22*). Electrostatic adhesion, although controllable and robust to different surfaces, provides relatively low adhesive pressures unless the voltage is very high, which can cause difficulties in control and is prone to damaging electronic components (*23*–*26*). In contrast, dry adhesives are passive. Some of these adhesives have been manufactured using space-grade low-volatility silicones and have been tested in a wide temperature range (*8*) and under radiation (*27*). See the Supplementary Materials for more details.

A variety of dry adhesives have been proposed over the last decade, and some of these produce high adhesive stresses; however, they typically require a relatively high force to engage and disengage with a surface (*28*–*30*). Microwedges, used in this work, are controllable dry adhesives with moderate normal adhesive stress and strong shear adhesive stress and with very low effort required to attach and detach (Fig. 1A) (*31*, *32*). When unloaded, the wedge-shaped adhesive fibers are slightly inclined with only the tips of the wedges contacting the surface. In this state, the van der Waals adhesion is negligible, and the adhesive is inactive or "off." When loaded in shear, the wedges bend over; contact area increases markedly, increasing shear adhesion capacity, and the adhesive is turned "on." When the shear load is removed, stored elastic energy returns the wedges to their neutral positions, reducing contact area and turning the adhesive off again. This behavior is observed for loads applied within about 20° of pure shear.

Previous work has demonstrated several approaches to gripping objects with dry adhesives. A soft inflatable gripper with fibrillar mushroom-tip adhesive was able to lift objects with different shapes (*33*, *34*). However, the pneumatic system does not work in space, and the adhesive requires a substantial engagement pressure. The integrated gripper presented here builds upon recently developed devices

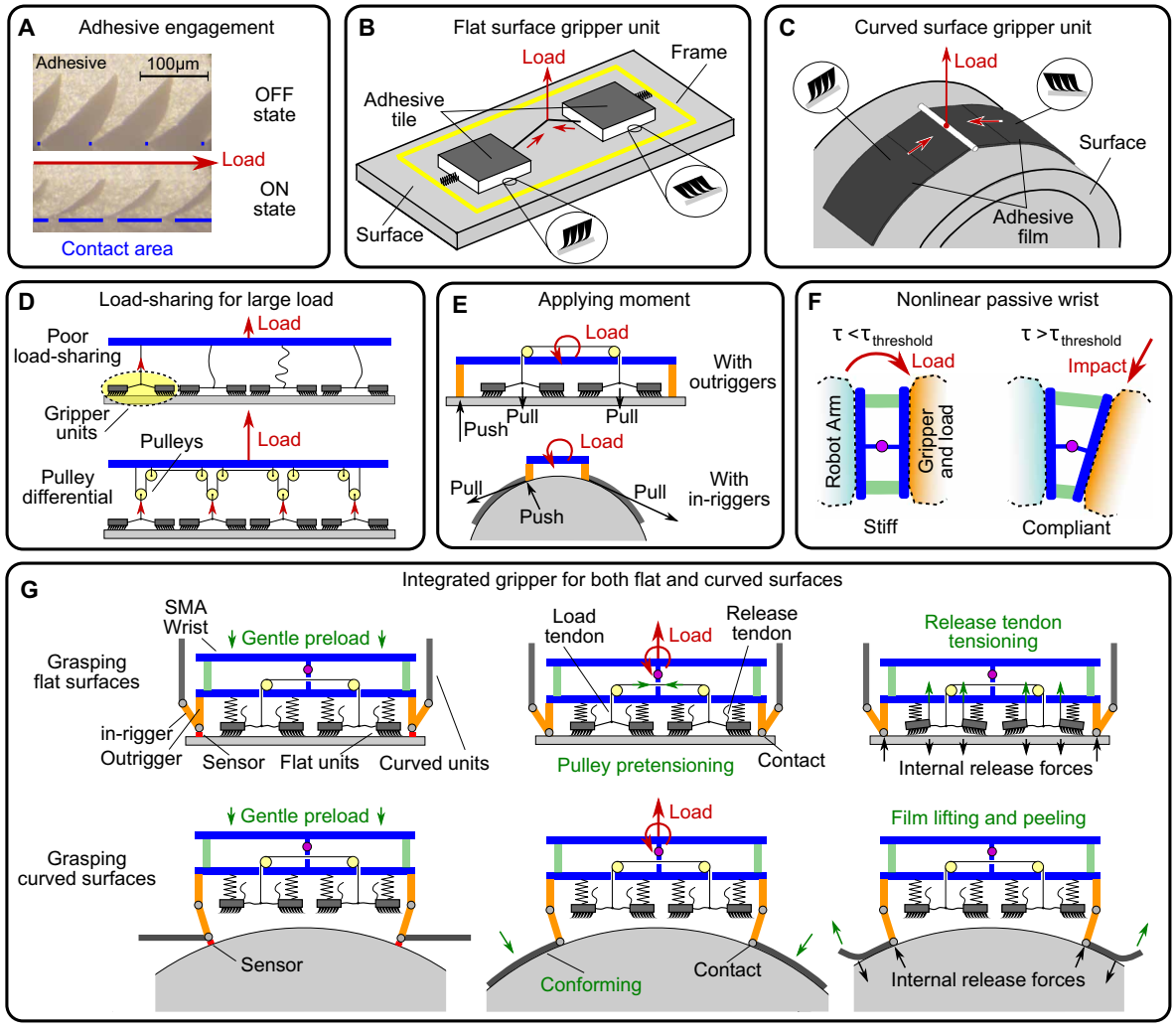

Fig. 1. Technologies in the integrated gripper: (**A**) Microscopic side views of the gecko-inspired controllable adhesive. (**B**) Flat gripper unit composed of two opposed adhesive tiles (*36*). (**C**) Curved unit of opposed, flexible adhesive films (*37*). (**D**) Load sharing using a pulley and tendon differential. (**E**) Applying moments with outriggers and in-riggers. (**F**) Wrist with nonlinear elements (in green) is stiff at light loads and compliant at larger loads. (**G**) Procedures for aligning, applying preload, applying forces and moments to manipulate, and releasing.

(shown in Fig. 1, B and C) that adhere to flat or curved surfaces with very low attachment and detachment forces (*35*–*38*). In both cases, the devices allow small patches of the adhesive to be loaded primarily in shear while combining their forces to support loads away from the surface. This capability makes the technology promising for use in microgravity, where it is essential not to disturb objects and send them off into different orbits.

Scaling the adhesive devices from a few square centimeters with a few newtons of adhesive force to more than a hundred square centimeters with tens of newtons of adhesive force requires load-sharing strategies, as illustrated in Fig. 1 (D and E). Otherwise, local stress concentrations due to surface defects or manufacturing tolerances will cause local adhesive failures that subsequently propagate across the entire contact. As a consequence, many adhesive systems, including that found in the gecko, exhibit a steady drop in available adhesive pressure with increasing area (*39*). Early versions of load-sharing systems are reported in (*32*, *39*, *40*); however, these are not suitable for use in space (e.g., due to using pneumatics or fluids), nor are they able to accommodate varying adhesive stresses that would be encountered for a range of materials, including metal and composite panels, solar cells, and insulating blankets.

We present an integrated gripper system that gently grasps large flat and curved objects using a combination of adhesives and load-sharing elements, sensors, actuators, and a nonlinear compliant wrist. We present models of the predicted capacity for applying force and moments in manipulation, which we confirm with tests in the laboratory and on free-floating platforms at NASA, and demonstrations aboard zero-gravity parabolic flights and in the International Space Station (ISS).

RESULTS

Integrated gripper design

As noted in Introduction, when scaling adhesion to large objects and areas, it is essential to ensure that forces are distributed evenly. The gripping system uses a tendon and pulley differential, shown schematically

in Fig. 1D. Because the tension in the tendon is approximately uniform, the gripping units, each consisting of two tiles with adhesives oriented in opposite directions, all experience the same load. If one unit fails, a hard stop prevents excessive slack, and the remaining units share the load without compromising the entire system. This feature makes the system functional on surfaces with defects.

For manipulating objects in space, it is desirable to impart forces and moments in any direction. The integrated gripper meets this requirement by combining flat and curved gripping elements in a distributed array. When applying moments, outriggers on flat surfaces and "in-riggers" on curved surfaces push against the surface as the adhesives pull and apply shear forces (Fig. 1E).

To acquire and manipulate objects, a wrist with nonlinear compliance is desirable. Compliance is required for absorbing energy and safely imparting forces and moments in the event of overloading; the compliance can help limit the force and moment applied to the adhesives. However, during manipulation, it is desirable to have a stiff wrist to minimize position errors and delays between commands on the arm and the gripper. The design of a nonlinear passive wrist that is stiff below a threshold torque is shown in Fig. 1F.

A functional diagram of the integrated space gripper is shown in Fig. 1G, and the computer-aided design (CAD) model and images of the gripper are shown in Fig. 2. It consists of eight flat gripper units and two sets of curved units to handle objects from 0.6 to 2.2 m in diameter and with a mass of up to 400 kg. When attaching to flat surfaces, the flat gripper units are pressed gently to make contact with the surface, and the pulley system is pretensioned to achieve a stiff grasp. For detaching, the tension is released, and, with no shear forces, the gripper units lose their adhesion. To further reduce detachment effort, we applied internal forces via release tendons (visible in Fig. 1G) that caused the flat tiles to peel as outriggers push against the surface. The curved gripper units are separated and can be deployed and retracted. Each pair of curved gripper "fingers" is connected with an independent pulley system. When attaching to curved surfaces, the bases of the fingers gently contact the surface and the film conforms. For detaching, the gripper fingers are opened. Again, the release force is internal, and there is negligible external force or vibration. There are two servo motors to control the pretensioning and releasing of the flat gripper units, three motors to control the deployment and retraction of the curved gripper units, and four motors for pretensioning the wrist. For testing purposes, we constructed the wrist with pitch and yaw axes instead of a full six degrees of freedom (DOFs). Four superelastic shape memory alloy (SMA) wires are used to create the nonlinear passive wrist. The wires are slack before grasping to allow the wrist to align freely with the object and are actively tightened after grasping, for manipulation. Four contact sensors are placed at the flat gripper outriggers and two are placed at the in-riggers to provide a signal indicating when the gripper is aligned with a surface. The integrated gripper has an automatic mode that detects contact and alignment and initiates a grasp; it also has a manual mode for triggering all functions.

Load-sharing element tests

Two four-unit flat grippers, one with a pulley differential mechanism and the other with tendons tied to a common panel, were built to test and compare load-sharing performance. The resulting normal adhesive forces of the individual units versus the total normal adhesion force of the entire gripper for five trials are plotted in Fig. 3A. The force profiles are normalized with respect to the maximum loads in each gripper. For the four-unit gripper with tendons tied to a panel, each unit has a substantially different load throughout the cycle due to the high tendon stiffness and small tendon length differences. The force profiles for different trials are not repeatable because the stiff system

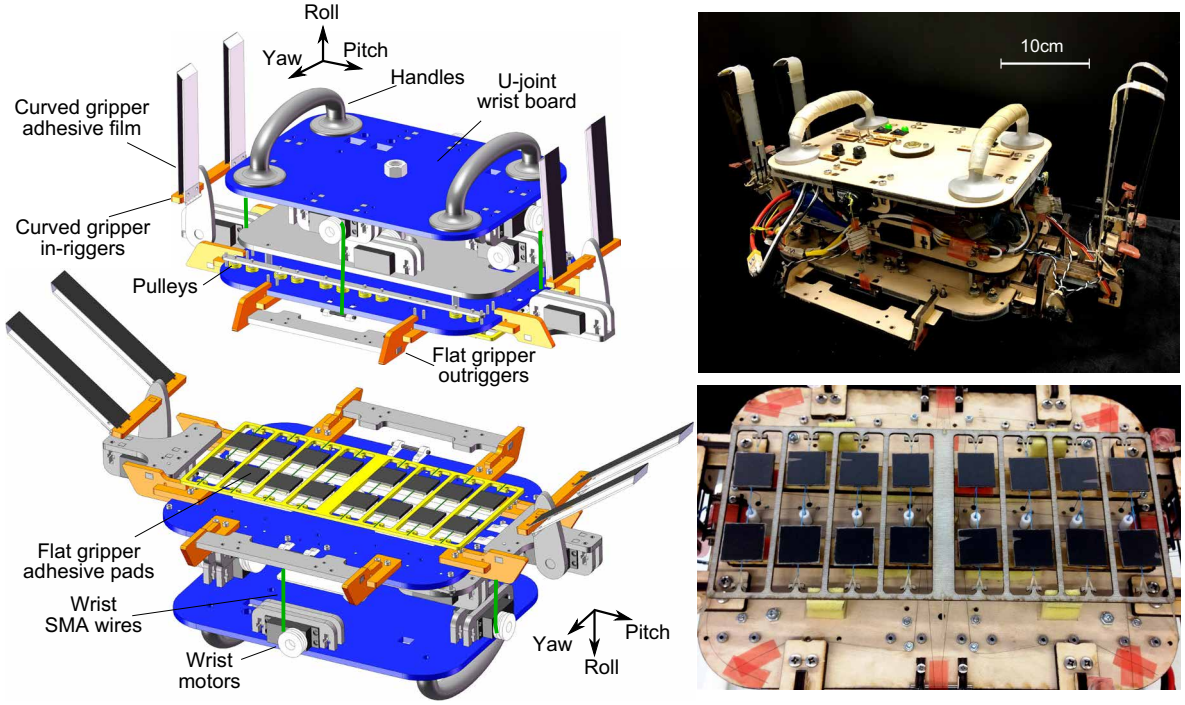

Fig. 2. Integrated gripper including eight flat gripper units and two curved gripper units. Servo motors control the pretensioning and release of gripping elements and SMA wrist wires.

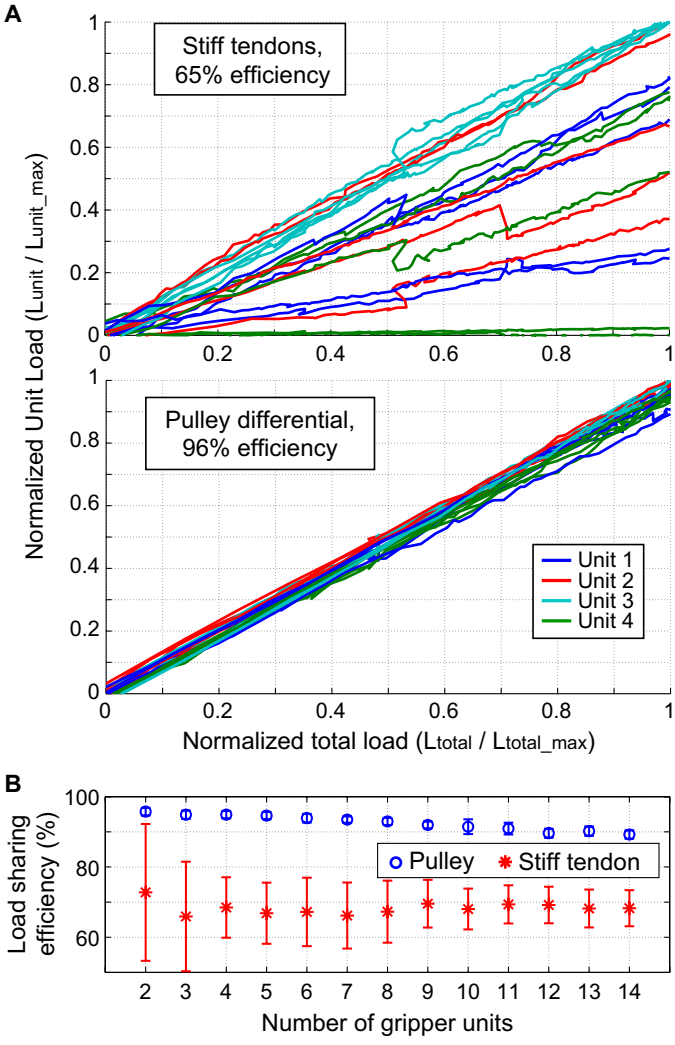

Fig. 3. Load-sharing results. (**A**) Force profiles for four flat gripper units and five trials with and without pulley differential [adapted from (*40*)]. (**B**) Load sharing reduces variability and improves load sharing; friction gradually reduces tendon/pulley performance.

is sensitive to slight changes in loading conditions. We define the load-sharing efficiency as $1 - \sigma/\mu$, where σ and μ are the SD and mean of the gripper units' loads, respectively. On average, this gripper achieves a load-sharing efficiency of 65%. The variance is initially high for different trials with few units and decreases as the number of units increases (Fig. 3B).

In comparison, the four-unit flat gripper with a pulley differential always shares the load evenly, as shown in the lower plot of Fig. 3A. On average, it achieves a 96% load-sharing efficiency. Further scaling results for up to 14 units are shown in Fig. 3B. Each data point corresponds to 20 measurements. Although the load-sharing efficiency drops slightly because of friction with increasing numbers of units, it continues to outperform a stiff system by a large margin. The variability in performance is also low across multiple trials, arising mainly from some variability in the pulley friction. For even higher numbers of units, hierarchical pulley systems can be used to mitigate friction accumulation.

Force limit tests and simulations

To evaluate the grasping and manipulation capability of the integrated gripper, we studied the gripper unit force capability and then extended it to combined force and moment capabilities. The adhesive force limit results of the flat gripper unit are shown in Fig. 4A. Each point on the surface corresponds to the magnitude of the force limit in the corresponding vector direction for five measurement trials. The SD is about 5%. The normal adhesion limit is 13 N, and the shear adhesion limits are 45 and 15 N. The tendon angles for the adhesive tiles are about 10°. The gripper unit has larger force capability in the x direction than in the y or z direction. This is because the x direction is the preferred loading direction of the adhesive wedges. A model for predicting such a limit surface, based on measurements from individual units and a given arrangement of tiles, can be found in (*36*).

For curved gripper units, the reaction forces can be very different with and without in-riggers. Here, we focus on the single adhesive film behavior as an element and then add both sides of the film together with in-riggers and outriggers when analyzing the combined force and moment capabilities. For the films, we define the adhesive coordinate frame as in Fig. 4B, such that x_{ad} is along the tangent of the film and y_{ad} is parallel to the cylinder axis. When loaded in shear in the preferred direction x_{ad}, the adhesive microwedge contact area increases as the load becomes larger. However, this monotonic trend is not linear. We can adapt data regarding adhesion versus adhesive contact area from (*41*), specifically the region from zero to maximum contact area. When the contact area is more than needed to support the actual load along the x_{ad} direction, there is extra adhesion capability left to support y_{ad} loads. We can use the measured area data and the ultimate shear capability in the preferred direction to develop a model for this y_{ad} adhesion capacity. This model is compared with measured data from a 645-mm^2 adhesive pad in Fig. 4B. The variation in data increases with increasing loads in x_{ad} because the system becomes increasingly sensitive to manufacturing imperfections; however, the model fits well enough for further force and moment analysis.

Because the adhesion limits of gripper units are not uniform in all directions, the layout of units affects the total adhesion. With perfect load sharing, the adhesive forces in all gripper units are identical. Hence, the adhesion of a gripper is limited by the unit with the lowest adhesion limit in the corresponding direction. Different possible arrangements are shown in Fig. 4 (C and D). For the case of a load in the x direction (denoted by the blue and cyan arrows), the red shade denotes the normalized unit loads. For the spoke arrangement, the units marked by blue dotted lines reach their limits first; hence, the entire gripper is limited by these two units. In contrast, with the rectangular array, all units reach their capacity at the same time. The corresponding adhesion limits of these layouts are shown in Fig. 4E. The limit surface of the tiled layout is a directly scaled version of the single unit, fit with an ellipsoid. The spoke layout has a hemispherical limit surface with a radius determined by whichever unit reaches its limit first. For arbitrary configurations, the gripper limits are given by the intersection of the unit limit surfaces transformed into gripper coordinates and scaled by the number of units. In general, the tiled layout with all the units in the same direction is more compact than other arrangements with the same minimum loads.

Combined force and moment modeling

To grasp and manipulate an object, combined force and moment limits in all loading directions need to be modeled and characterized. For clarity of presentation, we decompose the analysis of forces and

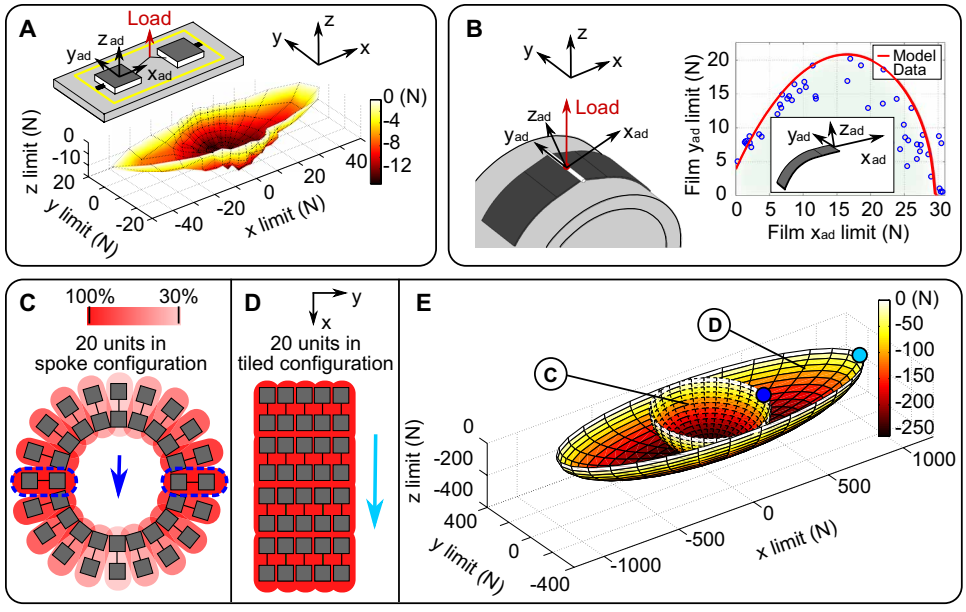

Fig. 4. Force limits and layout design. (**A**) Limit surface for a single flat gripper unit represents maximum pulling forces in each direction. (**B**) Two-dimensional force limit curve for flexible film on a curved surface. (**C**) Radial layout with 20 flat gripper units is limited by units in blue dashed ovals. Red shading represents percentage of each unit's maximum load. (**D**) Rectangular layout: All units contribute equally and overall limit surface is isomorphic to (A). (**E**) Ellipsoidal fits to limit surfaces for radial and rectangular layouts. Dots correspond to the load limits for blue and cyan vectors in (C) and (D).

moments into three orthogonal planes. As before, *x* corresponds to the preferred loading direction of the gripper units, and *z* is perpendicular to the surface. In each planar projection of the overall limit surface, we have two forces and a moment.

For the flat gripper element, the moments about the *x* and *y* axes are balanced by pushing on the outriggers and pulling on the gripper units. The moment about the *z* axis is balanced by load differences among the individual gripper units. With the pulley differential mechanism, all units should share the load; in practice, this moment is balanced by hard stops in the pulley system. For the curved gripper element, the moment about the *y* axis is balanced by the adhesive film and the inriggers. Because of the curvature, the pushing forces have different directions. For grasping cylindrical surfaces, there is no curvature about the *x* axis, and the moment analysis is the same as that for the flat gripper. Moments about the *z* axis are balanced by differences in the adhesion between different film pieces, again similar to the case for the flat gripper element. Thus, there are three different loading cases to model: (i) the flat gripper *x*-*z* plane loading, (ii) the flat gripper *x*-*y* plane loading, and (iii) the curved gripper *x*-*z* plane loading. Detailed analyses of the cases are provided in the Supplementary Materials. The overall limit surfaces representing the maximum force and moment capabilities of both flat and curved gripper elements are obtained such that the sum of the external forces and the extra forces caused by the external moments satisfies the gripper units' three-dimensional (3D) adhesion limit surfaces.

Combined force and moment tests

A four-unit flat gripper with a pulley differential load-sharing mechanism (a subset of the integrated gripper) was built to verify the flat gripper model. The modeled gripper reaction force and moment capability in the *x*-*z* plane are shown in Fig. 5A. Vertices in the polyhedral model arise from the contribution or absence of various force and moment components, as well as which adhesive pads reach their limits first. Four loading scenarios corresponding to vertices B to E are illustrated in Fig. 5 (B to E). In the schematics, the actual loads are on a wrist point above the surface, and the limit surface in Fig. 5A shows the reaction forces and moments with respect to a coordinate frame located at the contact centroid and aligned with the gripper coordinate frame. The apparent discontinuity at the edges for small values of *y* and large values of *x* is an artifact of the numerical simulation and depends on the simulation step size. In the experiment, 20 limit measurements were conducted to traverse the modeled domain, only in the first quadrant because of symmetry. The exact position of the loading point on the surface does not matter because the reaction force and moment combinations are evaluated at the center of the surface to align with the model. The comparison between the modeled limit surface and the measured data points is shown in Fig. 5A. The mean and SDs of the residuals between the model and the experiments were calculated on the basis of the combined force and moment magnitudes and tabulated in Fig. 5K.

A curved gripper with two adhesive film pieces on each side (again, a subset of the integrated gripper) was tested for comparison with the limit surface in the *x*-*z* plane shown in Fig. 5F. The limit surface is not symmetric about the *z* axis for all four quadrants but is symmetric about the origin. The surface has distinct regions corresponding to four reaction force scenarios and which side of the adhesive film reaches its limit first (six limit scenarios in total). Example transitional points are shown in Fig. 5 (G to J). Again, the actual loads act on a wrist point above the surface, and the limit surface in Fig. 5F is with respect to a coordinate frame located at the tangent intersection point and aligned with the gripper coordinate frame. For some vertices, there are only two reaction forces involved in the transitions. Measured forces and moments were transformed to the same coordinate frame as the limit surface. Forty-five data points were recorded to traverse the *y*+ side of the limit surfaces. The measured data are plotted against the modeled limit surface in Fig. 5F. Experiments do not cover the entire half of the limit surface because of the load limit of the force sensor, but the measured points provide good support for the model where data exist. Again, the mean and SDs of the residuals between the model and the experiments are calculated on the basis of the combined force and moment magnitudes and tabulated in Fig. 5K.

For the remaining loading planes, 20 to 30 experimental measurements were conducted to cover the modeled domain for each plane, and the mean and SD of the residuals are listed in Fig. 5K. Detailed limit surfaces for all six loading planes for both grippers are provided in movies S1 to S6.

The residuals between the model and experiments have a typical mean of 5% and an SD of 10 to 20%. In applications, one can choose an appropriate safety factor based on the model error to provide guidance

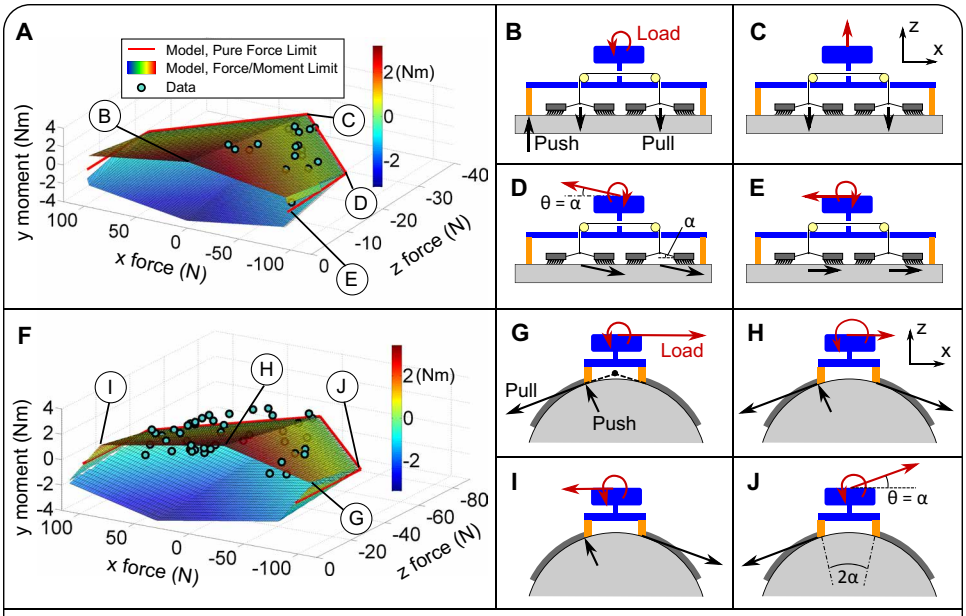

K

Model error	x-z (shear-normal) plane		y-z (shear-normal) plane		x-y (shear) plane	
Type	Mean	SD	Mean	SD	Mean	SD
Flat	5.0%	11.5%	5.0%	9.4%	3.1%	9.6%
Curved	4.8%	20.0%	5.3%	16.3%	2.6%	16.5%

Fig. 5. Comparison of predicted and measured forces and moments. (**A**) Flat gripper array: measurements taken in one quadrant, assuming symmetry. Labeled vertices B to E correspond to loading scenarios in (**B**) to (**E**), respectively. (**F**) Curved gripper array: measurements taken in two quadrants, assuming symmetry. Labeled vertices G to J correspond to loading scenarios in (**G**) to (**J**). (**K**) The residuals between the model and data for all loading planes. Additional loading scenarios and limit surfaces are included in the Supplementary Materials.

for gripper design and control. Generally, the model error is larger for curved grippers than for flat grippers. For all the gripper tests, there is always an error arising from uncertainties in the adhesion due to microscopically nonideal surface contact and manufacturing imperfections. This type of error is usually within 10%. The uncertainty of friction in the pulley differential system adds more variance to the measurement. In addition, with high loading forces and moments, the geometry of the gripper can change slightly because of tendon stretch and frame flexing, which contribute to errors. This is more obvious in the curved grippers than in the flat grippers because the adhesive film is more stretchable than rigid tiles. Furthermore, compared with flat grippers, curved grippers can misalign with cylindrical surfaces with a slight rotation about the *z* axis and thus reduce the adhesive contact area. This effect is evident for the curved gripper fingers that are reinforced with fiberglass sheets. Thus, the curved gripper model tends to have more error than the flat gripper.

Nonlinear wrist analysis and tests

For precise manipulation and adhesive overload protection, it is desirable that the wrist has a two-stage stiffness: high stiffness for precise manipulations while loads are safely within the adhesive's limits, then low stiffness as forces threaten to overcome these limitations. For energy absorption, the wrist needs to have substantial loading and unloading hysteresis, as found in SMA (Fig. 6A). For both loading and unloading cases, there is a two-stage stiffness where the first modulus is much higher than the second. An even higher initial stiffness can be achieved by pretensioning the wire. A simplified model of the loading and unloading curve of a pretensioned SMA wire is illustrated in the gray shaded region. A schematic of a one-DOF rotational wrist with pretensioned SMA wires is shown in Fig. 6B. The SMA wires are pretensioned with stop bars, ensuring that the wire is always in tension and then connected to strings. When the wrist rotates, one SMA wire extends, whereas on the other side, the string becomes slack. This design yields a nearly constant torque in both directions, a large hysteresis during loading and unloading cycles, and a nearly zero steady-state position error.

Spring dampers offer an alternative solution. Although a wrist with viscous damping absorbs energy well, it is not capable of stiff manipulation during gentle motions because its compliance is linear. It also does not provide ideal overload protection for an impulsive load because the total force is velocity-dependent. Nevertheless, it is useful as a baseline for comparing the energy absorption possible with the SMA wrist. Note that the gripper mounted to the wrist has force and moment limits, which impose maximum force and moment constraints on the wrist during energy dissipation. Given the same kinetic energy dissipation requirement, we use three criteria to compare different wrist designs: peak deflection, peak time, and settling time. For simplicity, we compare the case of a one-DOF wrist with a single adhesion limit in that direction. A multiple-DOF wrist, whether coupled or decoupled in the Cartesian space, with the corresponding adhesion limits in each direction, has similar behaviors and can be analyzed equivalently. Detailed analysis of the energy absorption comparison between the two types of wrists can be found in the Supplementary Materials.

A performance comparison for any force/torque constraint and input energy is listed in Fig. 6C. A simulated performance comparison between the SMA wrist and a critically damped spring-damper wrist with the same peak torque of 2.8 N·m and input energy of 0.087 J is shown in Fig. 6D. In the simulation, parameters of the integrated gripper are used, and the grasped object has a mass of 10 kg and a moment of inertia of 2.5 kg·m^2. A series of experiments were conducted with one-DOF SMA and spring-damper wrists, where a steel ball is launched at each wrist, which deflects and rebounds. Again, the torque constraint for both wrists is the same. A measurement comparison of the two wrists for dynamic impact is shown in Fig. 6E. In static loading conditions, the SMA wrist can perform stiff grasping and manipulation, whereas the spring-damper wrist is compliant and cannot transmit a force without deflection. In dynamic loading conditions with the same initial conditions, the SMA wrist requires much less total deflection and time to fully absorb the kinetic energy than the spring-damper wrist. Each wrist was measured for 10 trials. The small SD in the experiments

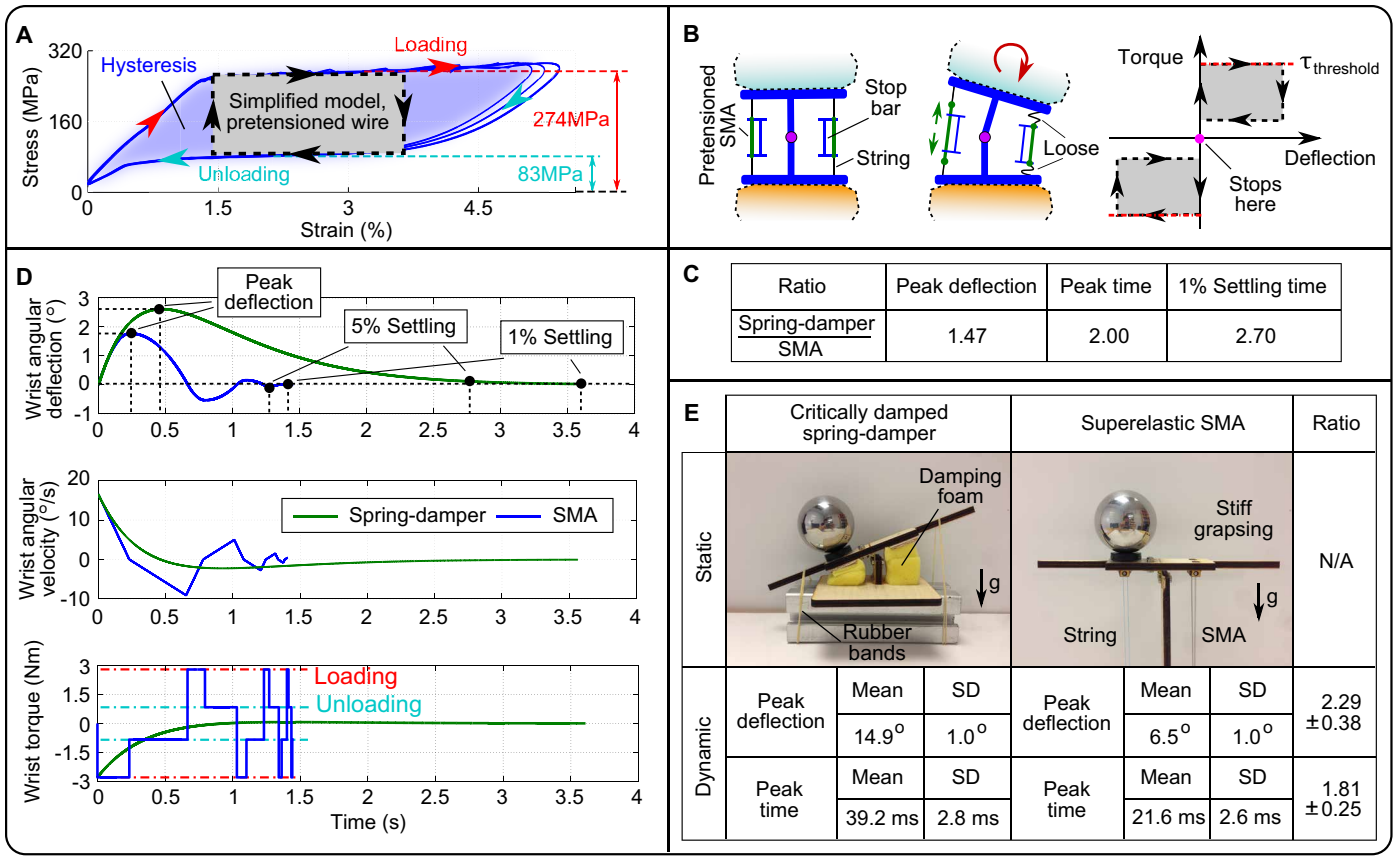

Fig. 6. Nonlinear passive wrist. (**A**) Loading and unloading curves for pretensioned superelastic SMA wire; energy loss approximated by the shaded rectangular region. (**B**) One-DOF wrist joint and corresponding torque/deflection model. SMA wire is connected to stop bars and flexible tendon strings, which are slack when unloaded. This design prevents deadband about the center. (**C**) Nonlinear wrist performance in comparison to critically damped linear system. (**D**) Simulation of wrist behavior in comparison to the spring-damper system. Initial energy and maximum torque are set equal in both cases. (**E**) Comparison of critically damped and SMA single-axis joints for absorbing energy from collision with a metal ball.

indicates that the SMA wrist consistently outperforms the spring-damper wrist for energy absorption by a factor of 2. The ratio of the specifications is slightly different from the predicted ratio in Fig. 6C. Error arises from high-speed video processing, flexing of the wrist structures, simplifications in modeling the SMA load curve, and nonlinearity in the damping coefficient.

One possible concern for SMA wires in application is that they will undergo fatigue with repeated phase transitions (*42*, *43*). The expected fatigue life is on the order of 1000 cycles with the constant force value, maximum strain, and total hysteresis decreasing as the number of cycles increases. In high-cycle applications, an alternative solution would be to use a brake with Coulomb friction and a soft spring. When the applied force is below the braking force, the wrist is rigid. Subsequently, it applies a force independent of velocity. When the brake is released, the spring returns the wrist to its center position.

Gripper system tests for application scenarios

Benchtop tests were conducted to determine the load capability and the preload and release forces of the integrated gripper. The gripper was mounted on a force sensor while target surfaces were pushed into it for preloading and pulled away for loading. Typical load cycles for flat and curved surfaces are shown in Fig. 7. The contact sensors were disabled for evaluation of the preload force. The flat and curved gripping elements were loaded to about 50% of their maximum capabilities. With five loading cycles for each surface, the maximum load-to-preload ratio for flat surfaces is 40:1 on average with an SD of 11:1 whereas that for curved surfaces is 53:1 on average with an SD of 10:1. The release forces are internal, producing no noticeable external forces. The maximum load-to-release vibration magnitude ratio is about 60:1 for both surfaces. In real applications, the contact sensors add up to 1 N more preload force. If the gripper is not fully aligned with the object, there can be a further preload required for alignment. However, these additional preload forces do not scale with the number of gripper units. The absolute load capability for the integrated gripper on either a flat glass panel or a 1-m-diameter aluminum cylinder is about 65 N in normal, 160 N in shear, and 6 N·m in moment. Unlike many terrestrial applications, grasping in a microgravity environment is not limited by the force magnitude but by the required acceleration of the manipulation task. The applied forces and moments are inertial. Particularly for robotic arm end effectors, even small grippers can manipulate arbitrarily large objects arbitrarily slowly. High rates of loading, which can decrease the maximum adhesion (*36*), are not discussed here because in all of the following application scenarios, the time from zero load to full load is more than 2 s. The large load-to-preload ratio and the load-to-release vibration ratio make the gripper a good candidate for grasping applications in space because it does not disturb objects.

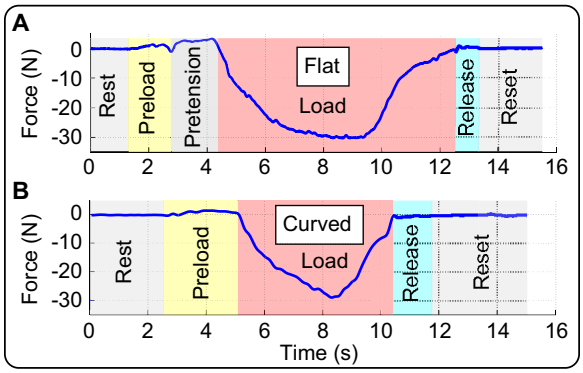

Fig. 7. Typical loading cycles of the integrated gripper. (**A**) Attachment to a flat glass plate. (**B**) Attachment to a 1-m-diameter spherical vinyl surface. Preloading denotes a process where the gripper is pushed into the surface to engage the gripper. Contact sensors are disabled to bypass their effects. During pretensioning on flat surfaces, motors eliminate slack in pulleys and cables. During release, forces are internal with negligible disturbance to object.

Experiments in microgravity were performed aboard NASA's C-9B aircraft, the Weightless Wonder, to test an integrated gripper grasping and manipulating a cube, a cylinder, and a sphere (Fig. 8, A and B). Because of aircraft space and safety requirements, the size and mass of the target objects are smaller than those of real satellites but still much larger than those of the gripper. A human manipulated the gripper to approach the free-floating cube and gently touched the cube to trigger the contact sensors. The maximum pushing distance is about 30 to 50 cm for a duration of 2 to 3 s. The maximum linear acceleration and the maximum angular acceleration during manipulation are about 0.1 m/s^2 and 0.5 rad/s^2, respectively. Release was triggered by the operator using a button, and the gripper detached from the cube without affecting its motion. Similar grasping and manipulating procedures were conducted with the cylinder and sphere, and similar grasping and manipulation performance was observed with the cylinder. The low mass of the sphere requires a very low engagement force to avoid pushing it away. The maximum manipulation acceleration on the sphere was about double that of the cube and cylinder. The success rate was 75% for the cube, 81% for the cylinder, and 100% for the sphere. The failures were due to excessive misalignment between the gripper and the objects caused by inaccurate positioning by the human operator or by the object bumping into obstacles that caused substantial disturbance. Zero-gravity grasping and manipulation cycles are shown in movie S7.

As a technology demonstration, handheld flat grippers were tested aboard the ISS in 2016 (Fig. 8C). Data collected by astronauts showed a strong correlation of adhesive forces to those collected on the ground, as expected. Long-duration use of the grippers was also demonstrated by leaving grippers in place for several weeks at a time. Additional lifetime tests have been conducted in the laboratory (*30*).

System-level dynamic testing was performed at NASA Jet Propulsion Laboratory's (JPL) formation control testbed using two floating robotic spacecraft, each with a mass of 370 kg and a moment of inertia of 46.3 kg·m^2. In the facility, both robots float on air bearings, providing frictionless relative motion and allowing grapple testing with representative masses and contact dynamics. During the experiment, one of the robots with a four-unit flat gripper (a subset of the integrated gripper) with a two-DOF SMA wrist chased and grappled a second robot as it drifted away with a solar panel exposed (Fig. 8D). The robots are more than 100 times larger than the gripper in volume. Upon impact, the gripper autonomously actuated, at which point the propulsive direction of the thruster system reversed, and the simulated debris was dragged to a desired location, stopped, and then released with a near-zero detachment force. Human-controlled grasping and manipulation were also demonstrated. For a variety of initial relative velocities in both orthogonal directions ranging from 0.05 to 0.15 m/s, the gripper was able to grasp and manipulate the target in more than 90% of the tests. When originally at rest, the target robot was pushed less than 5 cm away. When drifting away, the target robot decelerated to rest within 6 s. The linear and angular accelerations during manipulation were about 0.04 m/s^2 and 0.004 rad/s^2, respectively. Failures were mostly due to aggressive deceleration under human control immediately after impact. The SMA wrist damped out energy within four oscillation cycles, remained stiff for regular manipulation, and stretched when the human operator or thrusters tried to overload the adhesives. This end-to-end demonstration is a step toward a fully autonomous spacecraft that could hunt for and remove the most dangerous orbital debris objects. Several of these demonstrations are shown in movie S7.

In a climbing application, similar grippers were built to integrate with the Lemur 3 robot (*44*) for microgravity mobility demonstrations. The goal of this test was to demonstrate the viability of an inspection and repair robot that could participate in servicing activities on the outside of large spacecraft like the ISS, telecommunication satellites, telescopes, and future long-duration human spacecraft. The robot crawled across simulated solar panels and radiator panel surfaces in a gravity off-load test setup (Fig. 8E). Some of these demonstrations are shown in movie S7.

DISCUSSION

Significance of the work

The integrated gripper and its subsystems are demonstrated to scale gecko-inspired adhesives to areas of more than 100 cm^2 and use them to manipulate up to 370-kg objects in free-floating environments. The low attachment and detachment forces and vibrations are especially desirable because the gripper does not disturb floating objects.

The proposed load-sharing mechanisms, gripper unit arrangements, and wrist design are not specific to gecko-inspired controllable adhesives. All dry adhesives, electrostatic grippers, and even arrays of suction cups when used in an atmosphere have corresponding limits and can benefit from the analysis approach and load-sharing mechanisms presented here. In every case, designing a single large unit intrinsically makes the gripper vulnerable to surface defects, whereas using many small units with load-sharing and overload-protection strategies increases the robustness of the system.

The technology readiness level (TRL) for low Earth orbit (LEO) applications of the adhesive material is 6, as it has been tested in a space environment including thermal vacuum and a high radiation. The gripper system is at TRL 4+; it has been tested as a system beyond a laboratory environment but requires additional relevant maturation tests (environments). Once mature, this technology could be used for astronaut assistance tools or robots, in-space assembly of large structures, satellite servicing, spacecraft inspection, autonomous rendezvous and docking, and orbital debris mitigation.

Next-step challenges

Although adhesion-based gripping systems are strong enough to grasp and manipulate large objects in space, such systems do not provide

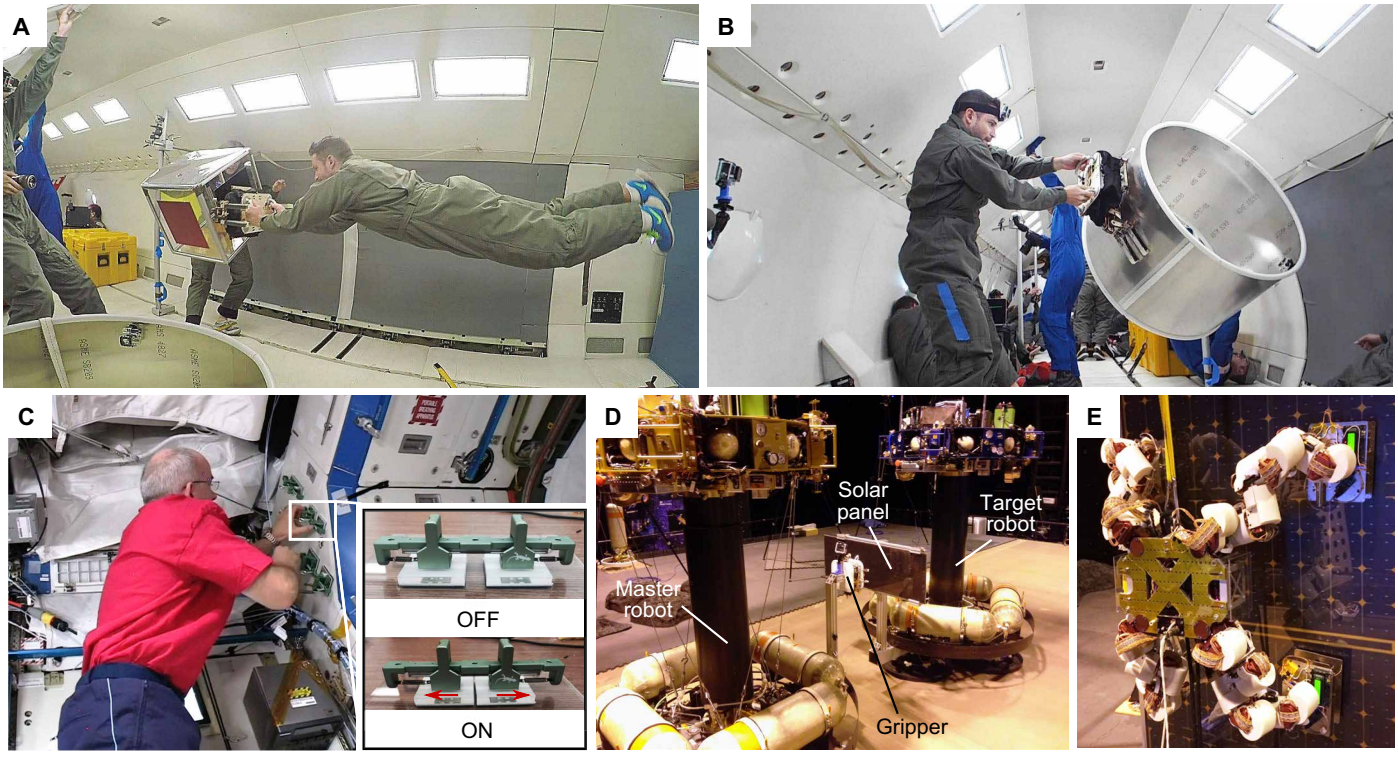

Fig. 8. Demonstrations integrated system tests. (**A** and **B**) Tests aboard zero-gravity airplane grasping and releasing large flat and curved objects. (**C**) Astronaut testing spring-loaded gripper units aboard the ISS. (**D**) Integrated system tests on large floating platforms at JPL: master robot captured target by gripping flat solar panels. (**E**) Lemur robot with four-unit flat gripper climbed a solar panel with gravity off-load.

grasping forces as large as those from grippers based on mechanical interlocking. Higher forces would allow higher accelerations, which might have advantages in certain scenarios. Accordingly, ongoing research involves modifying the design of the adhesive microstructures for larger adhesion capability.

Another issue is that the adhesion limit changes with loading direction and surface conditions, but the current SMA wrist is tuned to a fixed force/torque plateau. To make the best use of adhesives, controlled frictional damping elements will be implemented to vary the force/torque plateau according to specific loading directions and surface conditions, which can be measured with sensors integrated into the adhesive (*41*).

Last, surface contamination in space could be caused by atomic oxygen erosion and redeposition of volatile materials, an issue that could worsen the longer a target has been in LEO. The current adhesives have difficulties attaching to surfaces that are rough and loose because of corrosion and the flaking of surface treatments [a potential concern in earth orbit (*45*)]. Although atomic oxygen is not present in geostationary Earth orbit where many high-value satellites are present, ongoing research seeks to improve the adhesive for such challenging surfaces.

MATERIALS AND METHODS

Adhesive tile and film manufacture

The adhesive pads used in the experiments are made with silicone adhesive structures (polydimethylsiloxane; Dow Corning Sylgard 170) bonded to a rigid or flexible backing, using a primer (Dow Corning PR-1200 RTV Prime Coat) to promote bonding. The microwedges are about 100 μm tall with a 50-μm spacing. The microwedge shapes are formed by creating a mold in soft wax and then cast onto a prepared backing, using the process detailed in (*46*) and (*47*). For rigid backing, we used two layers of 1.14-mm-thick fiberglass sheet laminated with EZ-Lam epoxy. For flexible film, we used a single layer of 25-μm-thick Kapton sheet. For films to support y_{ad} axis loading, we added a single layer of 0.25-mm-thick fiberglass to the Kapton backing to increase resistance to lateral-torsional buckling.

Gripper manufacture

Both the flat and curved gripper units used Power Pro Spectra fishing lines as tendons to connect opposed adhesive tiles or film together. For the stiff tendon load-sharing implementation, the same fishing lines were used as loading tendons. V-groove ball bearings were used for the pulley differential load-sharing mechanism. The structure of the integrated gripper was made of 6-mm plywood. Power HD 1501MG servo motors were used for gripper deployment and retraction, gripper pretensioning and releasing, and SMA wrist pretensioning and fine-tuning. The contact sensors on the outriggers and in-riggers are contact switches with 50-mm-long triggering arms. The grippers were controlled with an Arduino MICRO.

Experimental setups

For load-sharing tests, the flat gripper, as a subset of the integrated gripper, has four units and a pulley differential mechanism. For the stiff tendon case, the pulley system is locked and disabled. Each gripper unit has two 645-mm^2 opposed adhesive tiles and can support

about 25 N in the *x* direction, 12 N in the *y* direction, and 8 N in the *z* direction on a flat glass surface. The outriggers in the *x* and *y* directions are spaced 190 mm apart. The spacings between adjacent gripper units are 34 or 42 mm in the *x* direction. We use individual glass tiles to mate with each adhesive tile, each instrumented with a Phidgets micro load cell, sampled at 10 Hz.

For force limit tests and simulations, the flat gripper unit for Fig. 4A consists of two 645-mm^2 opposed tiles with posttreated adhesives, and the adhesive patch for Fig. 4B has an adhesive area of 645 mm^2. The simulation shown in Fig. 4 (C to E) uses 20 flat gripper units that are the same as those in Fig. 3A in different layout patterns.

For combined force and moment tests, the flat gripper setup is the same as that used in load-sharing tests. The curved gripper setup has two 63 mm × 37 mm adhesive film pieces on each side of the gripper. The spacing between the two film pieces on each side is 30 mm. The adhesive film is reinforced with 0.25-mm-thick fiberglass backing such that the film is still flexible enough to conform to surface curvatures but rigid enough to suppress buckling in the lateral-torsional direction under a load in the y_{ad} axis. The outriggers are spaced 78 mm apart in the *x* direction and 116 mm in the *y* direction. The base of the adhesive film aligns with the outriggers in the *x*-*z* plane. Load sharing for the *x* and *z* axes is achieved with a pulley system, whereas the load sharing in the gripper *y* axis is decoupled from the other two axes to isolate the film y_{ad} axis loading from the x_{ad} axis loading. The gripper *y* axis load sharing was achieved with independent springs on the y_{ad} axis of each film piece. The diameter of the cylinder object is 211 mm, and the cylinder has an as-rolled aluminum surface. We use an ATI Gamma SI-130-10 sampling at 1000 Hz and unfiltered for force/torque measurements.

For nonlinear wrist tests, a single rotational DOF, superelastic SMA wrist joint was constructed to compare with a critically damped spring-damper wrist. The SMA wrist has six strands of 0.1-mm-diameter SMA wire on one side with a total force plateau of 45 N and a stiff string on the other side to pretension the wires. The distance between the SMA wire and the center of rotation is 30 mm, resulting in a torque plateau of the wrist of 1.35 N·m. For static loading comparisons, the spring-damper wrist is made of preloaded damping foam and rubber bands for simplicity. For dynamic loading comparisons, the spring damper is made of airpot dampers and rubber bands for better controlled damping. On the basis of the mass and inertia of wrist, the spring constant and damping coefficient of the spring dampers are adjusted to be critically damped. Both wrists are able to rotate through about 30°; we use only one side of the rotation in the experiment. The target object (a steel ball) has a mass of 0.55 kg with an impact point on the wrist, offset from the center of rotation for 90 mm; the rotational damping coefficient is 0.24 N·m·s/rad; and the torsional spring constant is 3.24 N·m/rad. The base of each wrist was fixed, and the ball was launched toward the wrist in a constrained channel in a horizontal plane. The incoming velocity of the ball has a mean of 0.51 m/s and an SD of 0.03 m/s, making the peak torque of both wrists the same. Given a peak torque limit, these two wrists represent the best values of stiffness and damping for each design. The process was recorded with an iPhone 7 camera at 240 frames per second.

The integrated gripper for benchtop and zero-gravity tests consists of eight flat gripper units, two curved gripper units, and a two-DOF SMA wrist. The eight flat gripper units are divided into two groups, each with four units spaced 34 mm apart. The groups are spaced 42 mm apart. The two film pieces of each flat gripper unit consist of two 645-mm^2 adhesive tiles. Each film piece has an area of 127 mm × 19 mm. The two adjacent film pieces on each side have a spacing of 50 mm. The SMA wires used in the wrist have a diameter of 0.15 mm and a force plateau of 9.3 N. Each side of the wrist has two strands of wire. The total rotation allowed for both pitch and yaw axes is about 20°. For benchtop experiments, we use an ATI Gamma SI-130-10 sampled at 200 Hz and filtered to 5 Hz. The force loading rates at about 2 N/s per tile were slow with respect to the adhesion limit and sampling rates. In the zero-gravity experiment, the cubic target consists of acrylic faces of 533 mm × 533 mm with a mass of 10.1 kg; the cylinder is a 6061 aluminum shell with a mass of 2.6 kg and a diameter of 1 m; the sphere is a 0.6-m-diameter air-pressurized plastic sphere. The gripper used in the test is shown in Fig. 2.

For tests in the ISS, each gripper unit pad is supported by a linear ball slide and biased with a spring to be in the on state. Each pad has ergonomic finger grips for ease of use; the gripper is turned off by squeezing these grips together. Once placed in contact, the grips are released and the bias spring loads the pads in shear, turning the gripper on. One-handed operation is therefore possible. These modifications are for ease of handling in the ISS and do not contribute to any performance difference. A total of five grippers of various sizes were demonstrated, two small units with 625-mm^2 pads, two medium units with 2500-mm^2 pads, and one large unit with 5800-mm^2 pads.

For tests on the air-bearing floor, the gripper is a subset of the integrated gripper, with four flat gripper units and a two-DOF SMA wrist. The flat gripper part is the same as that used in load-sharing tests, and the wrist is the same as that in the integrated gripper. The solar panel on the target robot has an attachable area of about 100 cm × 30 cm. Each of the master and target robots has a mass of 370 kg and an inertia of 46.3 kg·m^2 about an axis perpendicular to the floor.

SUPPLEMENTARY MATERIALS

robotics.sciencemag.org/cgi/content/full/2/7/eaan4545/DC1
Materials
Methods
Movie S1. The force and moment limit surface of a four-unit flat gripper in the *x*-*z* (shear-normal) plane.
Movie S2. The force and moment limit surface of a four-unit flat gripper in the *y*-*z* (shear-normal) plane.
Movie S3. The force and moment limit surface of a four-unit flat gripper in the *x*-*y* (shear) plane.
Movie S4. The force and moment limit surface of a two-unit curved gripper in the *x*-*z* (shear-normal) plane.
Movie S5. The force and moment limit surface of a two-unit curved gripper in the *y*-*z* (shear-normal) plane.
Movie S6. The force and moment limit surface of a two-unit curved gripper in the *x*-*y* shear plane.
Movie S7. Demonstration of the 2D and 3D floating tests of the grippers.
Reference (*48*)

REFERENCES AND NOTES

1. M. Garcia, Space debris and human spacecraft (2016); www.nasa.gov/mission_pages/station/news/orbital_debris.html.
2. NASA Orbital Debris Program Office, The orbital debris quarterly news; https://orbitaldebris.jsc.nasa.gov/quarterly-news/newsletter.html.
3. A. Parness, T. Hilgendorf, P. Daniel, M. Frost, V. White, and B. Kennedy, Controllable on-off adhesion for earth orbit grappling applications, in *2013 IEEE Aerospace Conference* (IEEE, 2013), pp. 1–11.
4. K. Wormnes, R. Le Letty, L. Summerer, R. Schonenborg, O. Dubois-Matra, E. Luraschi, A. Cropp, H. Krag, and J. Delaval, ESA technologies for space debris remediation, in *Proceedings of the 6th IAASS Conference: Safety is Not an Option* (IAASS, 2013), pp. 3–4.
5. N. Zinner, A. Williamson, K. Brenner, J. Curran, A. Isaak, M. Knoch, A. Leppek, J. Lestishen, Junk hunter: Autonomous rendezvous, capture, and de-orbit of orbital debris, in *Proceedings of AIAA SPACE 2011 Conference & Exposition* (AIAA, 2011), p. 7292.

6. L. Felicetti, P. Gasbarri, A. Pisculli, M. Sabatini, G. B. Palmerini, Design of robotic manipulators for orbit removal of spent launchers' stages. *Acta Astronaut.* **119**, 118–130 (2016).
7. A. Alessandro, New tool provides successful visual inspection of space station robot arm (2016); www.nasa.gov/mission_pages/station/research/VIPR.
8. A. Parness, M. Heverly, E. Hilgemann, D. Copel, N. Wettels, T. Hilgendorf, V. White, B. Kennedy, On-off adhesive grippers for earth-orbit, in *AIAA SPACE 2013 Conference and Exposition* (AIAA, 2013), p. 5533.
9. Jet Propulsion Laboratory, Gecko grippers moving on up (2015); www.jpl.nasa.gov/news/news.php?feature=4688.
10. D. A. Whelan, E. A. Adler, S. B. Wilson, G. M. Roesler Jr., Darpa orbital express program: Effecting a revolution in space-based systems. *Proc. SPIE* **4136**, 48–56 (2000).
11. R. Friend, Orbital express program summary and mission overview. *Proc. SPIE* **6958**, 10.1117/12.783792 (2008).
12. C. Melchiorri and M. Kaneko, Robot hands, in *Springer Handbook of Robotics* (Springer, 2016), pp. 463–480.
13. A. Chiesa, F. Fossati, G. Gambacciani, E. Pensavalle, Enabling technologies for active space debris removal: The cadet project, in *Space Safety Is No Accident* (Springer, 2015), pp. 29–38.
14. T. Debus, S. Dougherty, Overview and performance of the front-end robotics enabling near-term demonstration (FREND) robotic arm, in *AIAA Infotech@ Aerospace Conference* (AIAA, 2009), p. 1870.
15. G. Gefke, A. Janas, R. Chiei, M. Sammons, and B. B. Reed, Advances in robotic servicing technology development, in *AIAA SPACE 2015 Conference and Exposition* (AIAA, 2015), p. 4426.
16. J. Ratti, Launch adapter ring (LAR) capture tool: Enabling space robotic servicing, poster presented at IEEE International Conference on Robotics and Automation (ICRA) (IEEE, 2015).
17. D. Ruffatto, D. Beganovic, A. Parness, M. Spenko, Experimental results of a controllable electrostatic/gecko-like adhesive on space materials, in *2014 IEEE Aerospace Conference* (IEEE, 2014), pp. 1–7.
18. M. Henrey, J. P. D. Téllez, K. Wormnes, L. Pambaguian, C. Menon, Towards the use of mushroom-capped dry adhesives in outer space: Effects of low pressure and temperature on adhesion strength. *Aerosp. Sci. Technol.* **29**, 185–190 (2013).
19. J. Purtov, M. Frensemeier, E. Kroner, Switchable adhesion in vacuum using bio-inspired dry adhesives. *ACS Appl. Mater. Interfaces* **7**, 24127–24135 (2015).
20. L. Heepe, M. Varenberg, Y. Itovich, S. N. Gorb, Suction component in adhesion of mushroom-shaped microstructure. *J. R. Soc. Interface* **8**, 585–589 (2010).
21. D. Sameoto, H. Sharif, C. Menon, Investigation of low-pressure adhesion performance of mushroom shaped biomimetic dry adhesives. *J. Adhes. Sci. Technol.* **26**, 2641–2652 (2012).
22. M. Henrey, J. Tellez, K. Wormnes, L. Pambaguian, C. Menon, Sticking in space: Manufacturing dry adhesives and testing their performance in space environments, in *12th Symposium on Advanced Space Technologies in Robotics and Automation* (ASTRA, 2013), pp. 15–17.
23. D. Ruffatto, A. Parness, M. Spenko, Improving controllable adhesion on both rough and smooth surfaces with a hybrid electrostatic/gecko-like adhesive. *J. R. Soc. Interface* **11**, 20131089 (2014).
24. D. Ruffatto III, J. Shah, M. Spenko, Increasing the adhesion force of electrostatic adhesives using optimized electrode geometry and a novel manufacturing process. *J. Electrostat.* **72**, 147–155 (2014).
25. J. Shintake, S. Rosset, B. Schubert, D. Floreano, H. Shea, Versatile soft grippers with intrinsic electroadhesion based on multifunctional polymer actuators. *Adv. Mater.* **28**, 231–238 (2016).
26. L. Savioli, G. Sguotti, A. Francesconi, F. Branz, J. Krahn, C. Menon, Morphing electroadhesive interface to manipulate uncooperative objects, in *SPIE Smart Structures and Materials + Nondestructive Evaluation and Health Monitoring* (SPIE, 2014), pp. 906129–906129.
27. P. Day, M. Cutkosky, A. McLaughlin, Effects of gamma irradiation on adhesion of polymer microstructure-based dry adhesives. *Nucl. Technol.* **180**, 450–455 (2012).
28. Y. Li, J. Krahn, C. Menon, Bioinspired dry adhesive materials and their application in robotics: A review. *J. Bionic Eng.* **13**, 181–199 (2016).
29. S. Kim, M. Sitti, Biologically inspired polymer microfibers with spatulate tips as repeatable fibrillar adhesives. *Appl. Phys. Lett.* **89**, 261911 (2006).
30. M. P. Murphy, S. Kim, M. Sitti, Enhanced adhesion by gecko-inspired hierarchical fibrillar adhesives. *ACS Appl. Mater. Interfaces* **1**, 849–855 (2009).
31. A. Parness, D. Soto, N. Esparza, N. Gravish, M. Wilkinson, K. Autumn, M. Cutkosky, A microfabricated wedge-shaped adhesive array displaying gecko-like dynamic adhesion, directionality and long lifetime. *J. R. Soc. Interface* **6**, 1223–1232 (2009).
32. E. W. Hawkes, E. V. Eason, A. T. Asbeck, M. R. Cutkosky, The gecko's toe: Scaling directional adhesives for climbing applications. *IEEE ASME T. Mech.* **18**, 518–526 (2013).
33. S. Song, C. Majidi, M. Sitti, GeckoGripper: A soft, inflatable robotic gripper using gecko-inspired elastomer micro-fiber adhesives, in *2014 IEEE/RSJ International Conference on Intelligent Robots and Systems (IROS)* (IEEE, 2014), pp. 4624–4629.
34. S. Song, D.-M. Drotlef, C. Majidi, M. Sitti, Controllable load sharing for soft adhesive interfaces on three-dimensional surfaces. *Proc. Natl. Acad. Sci. U.S.A.* **114**, E4344–E4353 (2017).
35. E. W. Hawkes, D. L. Christensen, E. V. Eason, M. A. Estrada, M. Heverly, E. Hilgemann, H. Jiang, M. T. Pope, A. Parness, M. R. Cutkosky, Dynamic surface grasping with directional adhesion, in *2013 IEEE/RSJ International Conference on Intelligent Robots and Systems (IROS)* (IEEE, 2013), pp. 5487–5493.
36. E. W. Hawkes, H. Jiang, M. R. Cutkosky, Three-dimensional dynamic surface grasping with dry adhesion. *Int. J. Robot. Res.* **35**, 943–958 (2016).
37. E. W. Hawkes, D. L. Christensen, A. K. Han, H. Jiang, M. R. Cutkosky, Grasping without squeezing: Shear adhesion gripper with fibrillar thin film, in *2015 IEEE International Conference on Robotics and Automation (ICRA)* (IEEE, 2015), pp. 2305–2312.
38. M. A. Estrada, B. Hockman, A. Bylard, E. W. Hawkes, M. R. Cutkosky, M. Pavone, Free-flyer acquisition of spinning objects with gecko-inspired adhesives, in *2016 IEEE International Conference on Robotics and Automation (ICRA)* (IEEE, 2016), pp. 4907–4913.
39. E. W. Hawkes, E. V. Eason, D. L. Christensen, M. R. Cutkosky, Human climbing with efficiently scaled gecko-inspired dry adhesives. *J. R. Soc. Interface* **12**, 20140675 (2015).
40. H. Jiang, E. W. Hawkes, V. Arutyunov, J. Tims, C. Fuller, J. P. King, C. Seubert, H. L. Chang, A. Parness, and M. R. Cutkosky, Scaling controllable adhesives to grapple floating objects in space, in *2015 IEEE International Conference on Robotics and Automation (ICRA)* (IEEE, 2015), pp. 2828–2835.
41. X. A. Wu, D. L. Christensen, S. A. Suresh, H. Jiang, W. R. T. Roderick, M. Cutkosky, Incipient slip detection and recovery for controllable gecko-inspired adhesion. *IEEE Robot. Autom. Lett.* **2**, 460–467 (2016).
42. G. Eggeler, E. Hornbogen, A. Yawny, A. Heckmann, M. Wagner, Structural and functional fatigue of NiTi shape memory alloys. *Mater. Sci. Eng. A* **378**, 24–33 (2004).
43. G. Kang, D. Song, Review on structural fatigue of NiTi shape memory alloys: Pure mechanical and thermo-mechanical ones. *Theor. Appl. Mech. Lett.* **5**, 245–254 (2015).
44. A. Parness, N. Abcouwer, C. Fuller, N. Wiltsie, J. Nash, B. Kennedy, Lemur 3: A limbed climbing robot for extreme terrain mobility in space, in *IEEE International Conference on Robotics and Automation (ICRA)* (IEEE, 2017), pp. 5467–5473.
45. A. Rooij, Corrosion in space, *Encyclopedia of Aerospace Engineering* (John Wiley & Sons, 2010).
46. P. Day, E. V. Eason, N. Esparza, D. L. Christensen, M. R. Cutkosky, Microwedge machining for the manufacture of directional dry adhesives. *J. Micro. Nano-Manuf.* **1**, 011001 (2013).
47. S. A. Suresh, D. L. Christensen, E. W. Hawkes, M. R. Cutkosky, Surface and shape deposition manufacturing for the fabrication of a curved surface gripper. *J. Mech. Robot.* **7**, 021005 (2015).
48. B. A. Banks, K. K. deGroh, S. K. Rutledge, C. A. Haytas, Consequences of atomic oxygen interaction with silicone and silicone contamination on surfaces in low earth orbit, *NASA Technical Reports Server* (1999).

Acknowledgments: We thank V. Arutyunov, J. Tims, J. P. King, R. Smith, C. Seubert, and H. L. Chang for help with the air-bearing floor and zero-gravity experiments. **Funding:** This work was partially supported by NASA under grants NNX12AQ43G and ESI NNX16AD19G. Research was carried out, in part, at JPL, California Institute of Technology, under a NASA contract. S.A.S. was supported by a NASA Space Technology Research Fellowship; M.A.E. was supported by the NSF Graduate Research Fellowship Program; A.K.H. was supported by a Samsung Scholarship. **Author contributions:** H.J. designed grippers for benchtop and floating tests, carried out the modeling, conducted experiments, and wrote the manuscript; E.W.H. advised and supervised the design and edited the manuscript; C.F. designed grippers for the Lemur robot and conducted relevant experiments; M.A.E. advised the modeling and edited the manuscript; S.A.S. advised the benchtop experiments and edited the manuscript; N.A. designed the Lemur 3 robot and conducted relevant experiments; A.K.H. helped with wrist experiments and edited the manuscript; S.W. and C.J.P. advised the wrist analysis and edited the manuscript; A.P. supervised the project, coordinated the 2D and 3D floating tests, and edited the manuscript; M.R.C. supervised the project, advised the design and experiments, and edited the manuscript. **Competing interests:** The authors declare that they have no competing interests. **Data and materials availability:** Contact H.J. for any questions regarding modeling codes and experiment data.

Submitted 15 April 2017
Accepted 9 June 2017
Published 28 June 2017
10.1126/scirobotics.aan4545

Citation: H. Jiang, E. W. Hawkes, C. Fuller, M. A. Estrada, S. A. Suresh, N. Abcouwer, A. K. Han, S. Wang, C. J. Ploch, A. Parness, M. R. Cutkosky, A robotic device using gecko-inspired adhesives can grasp and manipulate large objects in microgravity. *Sci. Robot.* **2**, eaan4545 (2017).

Science Robotics

A robotic device using gecko-inspired adhesives can grasp and manipulate large objects in microgravity

Hao Jiang, Elliot. W. Hawkes, Christine Fuller, Matthew A. Estrada, Srinivasan A. Suresh, Neil Abcouwer, Amy K. Han, Shiquan Wang, Christopher J. Ploch, Aaron Parness, and Mark R. Cutkosky

Sci. Robot. **2** (7), eaan4545. DOI: 10.1126/scirobotics.aan4545

Science Robotics (ISSN 2470-9476) is published by the American Association for the Advancement of Science. 1200 New York Avenue NW, Washington, DC 20005. The title *Science Robotics* is a registered trademark of AAAS.